Supporting Information

Melt-Sintering of MOF Glass–2D Nanosheet Composites for Enhanced Processability and Gas Separation Performance

Jie Yang [a], Shuke Zhao [a], Wengang Huang [a], Bun Chan [d], Zhonghao Xu [c], Meilin Yin [a], Weikang Lin [e], Milton Chai [a], Rijia Lin [a], Shuwen Yu [f], Mingyuan Lu [e], Wei Li *[b], Xiwang Zhang [c], Vicki Chen [a], Jingwei Hou*[ac]

[a.] Nanomaterials Centre, School of Chemical Engineering, The University of Queensland, St Lucia, Queensland 4072, Australia

[b.] School of Material Science and Engineering, Nankai University, Tianjin 300071, China

[c.] ARC Centre of Excellence for Green Electrochemical Transformation of Carbon Dioxide, Brisbane, 4072 Australia

[d.] Graduate School of Engineering, Nagasaki University, Nagasaki 852-8521, Japan

[e.] School of Mechanical and Mining Engineering, The University of Queensland, St Lucia, Queensland 4072, Australia

[f.] Nanomaterials Centre, School of Chemistry and Chemical Engineering, Suzhou University, Suzhou, 234000, China

Email address of the corresponding author:

Wei Li: wl276@nankai.edu.cn

Jingwei Hou: jingwei.hou@uq.edu.au

Table of Contents

Experimental Methods Section

1.1 Materials

All chemicals were commercially available without further purification. $Zn(NO_3)_2 \cdot 6H_2O$, imidazole(Im), benzimidazole (bIm), melamine, N,N-dimethylformamide (DMF), Dichloromethane (DCM), ethanol, 2-isopropanol were purchased from Sigma-Aldrich.

1.2 Methods

Synthesis of g-C_3N_4:

Pristine g-C_3N_4 was synthesized via the direct thermal polycondensation of melamine. Typically, 10 g of melamine powder was placed in a covered alumina crucible and heated to 550 °C in an air atmosphere at a ramping rate of 3 °C min^{-1}. The temperature was maintained at 550 °C for 6 h to ensure complete condensation, followed by natural cooling to room temperature at the same rate. The resulting light-yellow product was collected, washed several times with ethanol by centrifugation to remove residual by-products. The obtained powder subsequently ultrasonically dispersed in ethanol collected by centrifugation and dried under vacuum at 60 °C for 24h.

Synthesis of ZIF-62:

ZIF-62 crystals were synthesized by a solvothermal method. Typically, $Zn(NO_3)_2 \cdot 6H_2O$ (1.2 g), imidazole (Im, 0.79 g), and benzimidazole (bIm, 0.196 g) were dissolved in 90 mL of N,N-dimethylformamide (DMF) and stirred for 30 min to obtain a homogeneous solution. The resulting solution was then transferred into a sealed Teflon-lined autoclave and heated at 130 °C for 72 h. After cooling to room temperature, the obtained crystals were collected by centrifugation, thoroughly washed with DMF and methanol three times, and finally dried in a vacuum oven at 150 °C for 24 h.

Fabrication of glass composites:

ZIF-62 crystal and g-C_3N_4 powder were mixed in mass ratios of 9:1, 7.5:2.5 and 6:4, respectively, for a total sample mass of 25 mg. Next, the ZIF-62 and g-C_3N_4 powders were ground in mortar with a slight amount of isopropanol to achieve a homogeneous mixture. After thorough mixing of the powders, the obtained mixture was transferred into a 7 mm diameter compression mould, and the composite pellets were shaped under a pressure of 8 MPa. The crystal pellets were denoted as ZIF-62_CN-x, where x is the mass percentage of g-C_3N_4.

The glass composite pellets were obtained by placing the pellet in a tube furnace and heating to 400, 420, 440, 450, 460°C for 30 min at 10 °C min-1 under Ar atmosphere and then cooling to room temperature. The glass composite pellets were denoted as a_gZIF-62_CN-x, where x is the mass percentage of g-C_3N_4.

1.3 Characterization

Liquid-state nuclear magnetic resonance spectroscopy

The Liquid-state 1H Nuclear Magnetic Resonance spectroscopy measurement (NMR) was performed with a Bruker Avance 500 high-resolution NMR spectrometer using a mixture of DCl/D_2O (35%) and DMSO-d_6.

Powder X-ray diffraction

X-ray diffraction (XRD) patterns were collected with a Bruker D8 Advanced X-Ray diffractometer (40 kV, 30 mA) using a Cu Kα (λ= 0.15406 nm) radiation source. For in-situ XRD experiments, the powdered sample was loaded into a quartz capillary of 700 μm diameter within a gas flow cell and measured using the Powder Diffraction beamline at the Australian Synchrotron facility. The flow cell was connected to a nitrogen gas flow line with temperature controlled via a hot air blower.

Scanning electron microscope

The morphology of crystal and glass composite samples was investigated using a JEOL JSM-7800 SEM with energy dispersive spectroscopy (EDS). The surface and interfacial

morphologies of the pellets before and after melting were observed by fracturing the samples to expose their internal cross sections.

Attenuated total reflection Fourier transform infrared spectroscopy

Fourier transform infrared (FTIR) spectra were collected in air using a Shimadzu IRTracer-100 spectrometer equipped with a GladiATR 10 single-reflection ATR accessory. The spectra were recorded over a wavenumber range of 400-4000 cm^{-1}.

X-ray photoelectron spectroscopy

X-ray photoelectron spectroscopy (XPS) survey and Zn 2p high-resolution spectra were acquired using a Kratos Axis Ultra Supra Plus spectrometer equipped with a monochromatic Al Kα X-ray source (hν = 1486.6 eV). The binding energy scale was calibrated against the C 1s peak at 284.8 eV.

Synchrotron Tera-Hz Far-Infrared (THz/FarIR) absorption spectroscopy

Synchrotron Tera-Hz Far-Infrared (THz/Far-IR) absorption spectroscopy was obtained at the Australian Synchrotron beamline with a Bruker IFS 125/HR Fourier Transform (FT) spectrometer. A multilayer Mylar beam splitter (6 μm) together with a liquid-helium-cooled bolometer detector was utilized to achieve a high signal-to-noise ratio. The samples were examined in attenuated total reflection (ATR) geometry employing a diamond crystal as the internal reflection element. Temperature-resolved synchrotron terahertz (THz) far-infrared (FarIR) vibrational in-situ spectroscopy was obtained using a heating stage integrated with the ATR module under a continuous argon flow (20 mL min^{-1}). All spectral acquisition and baseline processing were conducted with the OPUS 8.0 software package.

Simulation method with density functional theory (DFT) calculations

To gain a deeper understanding of the THz spectral features, density functional theory (DFT) calculations were performed. Quantum-chemical calculations were primarily conducted using the xTB program[1], chosen for its balance between adequate accuracy and exceptional

computational efficiency, an essential factor for simulating the relatively large models employed in this study. The GFN2-xTB method (XTB2) was adopted as the default computational scheme[2]. In the preliminary stage, smaller molecular models were also investigated using the more rigorous ωB97X-3c functional[3] to validate the reliability of the XTB2 approach[4]. These calculations were carried out with the ORCA software package. Subsequently, a series of larger models (comprising up to >500 atoms) were examined to evaluate the influence of system size on the computed vibrational properties. The Zn–N distance distributions in the larger cluster models were extracted from the optimized structures obtained using the same GFN2-xTB protocol.

Synchrotron X-ray total scattering

Zn K-edge X-ray absorption spectroscopy (XAS) measurements were conducted at the XAS beamline of the Australian Synchrotron (ANSTO). Synchrotron Extended X-ray absorption fine structure (EXAFS) was collected in transmission mode at the μSpot beamline of the synchrotron BESSY-II. A Zn metal foil was simultaneously recorded downstream of the sample for energy calibration. Data reduction and analysis were carried out using the Demeter XAS software suite. Background subtraction, normalization, and conversion to k-space were performed in Athena, followed by Fourier transform and EXAFS modeling in Artemis.

Mechanical measurements

The elastic modulus (E) of the composite glass samples was measured using a Hysitron Triboindenter (Hysitron Inc., Minneapolis, MN, USA), equipped with a Berkovich probe. Nanoindentation measurements were conducted using a Berkovich diamond tip under load-control mode with a maximum applied load of 1 mN and a loading-holding-unloading sequence of 10 s, 5 s, and 15 s, respectively. The samples were mounted in epoxy resin, ground and polished.

High-resolution transmission electron microscopy

High-resolution transmission electron microscopy (HRTEM) was performed on a Hitachi HF5000 Cs-corrected STEM/TEM (Japan) operated at 200 kV to characterize the morphology and lattice of selected regions of the glass composite. HRTEM images were recorded on the same instrument at 200 kV, and image processing/analysis was carried out using Gatan DigitalMicrograph software. Lattice-fringe spacings were measured from inverse fast Fourier transform (IFFT)-filtered images obtained from the corresponding FFTs to enhance fringe visibility and accuracy.

Thermogravimetric analysis and Differential scanning calorimeter

Thermogravimetric analysis (TGA) was conducted using a Mettler Toledo TGA/DSC System. To determine the melting and decomposition temperature, the sample was heated at a rate of 20 °C min^{-1} under an N_2 atmosphere to 800 °C. Differential scanning calorimeter (DSC) curve was obtained on NETZSCH DSC 214 instrument. For the DSC test, the samples were heated for two scan cycles. In scan 1, the sample is heated from 50 °C to 500 °C in an Ar atmosphere at 10 °C min^{-1}. Immediately after cooling at a rate of 50 °C min^{-1}, the sample is subjected to scan 2, which follows the same procedure as in scan 1 and heated to 430 °C.

Gas adsorption analysis

The CO_2 adsorption isotherms at 273K and 298K using a Micromeritics TriStar II 3020. For the BET surface areas, the CO_2 adsorption isotherms at 195 K were recorded on ASAP 2020 with a ColdEdge cooler. Before the test, all the samples were degassed at 150 °C for 24 h. The isosteric heat of CO_2 adsorption was calculated by the following equation using the measured CO_2 adsorption data at 273 K and 298 K, where R is the universal gas constant, P and T depends on the equilibrium pressure and temperature, respectively

$$Q_{st} = \frac{RT_1T_2\ln\left(\frac{P_2}{P_1}\right)}{T_1 - T_2}$$

Gas permeation measurement

The single gas permeation performance of membranes for CO_2, H_2, N_2 and CH_4 was evaluated at 30 °C through a constant volume permeation system with variable feed pressure with the use of a laboratory-customized stainless steel membrane module. And the trans-membrane pressure was about 1 bar during the test. The permeation coefficient (P in GPU) is estimated to follow the equation:

$$P = \frac{\frac{273.15 \times 10^{10}}{760AT} \cdot \frac{V\frac{dp}{dt}}{P_0 \times 76}}{14.7}$$

where A is the effective test membrane area (cm^2), T is the measurement temperature (K), V is the dead volume of the permeation side (cm^3), P_0 is the feeding pressure (psi). 1 GPU =1×10^{-6} cm^3(STP) cm^{-2} s^{-1} $cmHg^{-1}$

The ideal selectivity for two gases was calculated according to the equation:

$$\alpha = \frac{P_A}{P_B}$$

The mixed-gas permeation measurements were performed using a Wicke–Kallenbach permeation apparatus. Equimolar H_2/CO_2 mixed gas (50:50 vol%) was supplied to the feed side with a total flow rate of 40 mL min^{-1}, while Ar was used as the sweep gas on the permeate side at a flow rate of 40 mL min^{-1}. The permeation tests were conducted at 30 °C and the composition of the permeate stream was continuously monitored using an online gas chromatograph (Shimadzu GC-2014).

The permeance of component *i* was calculated according to:

$$P_i = \frac{N_i}{A\Delta P_i}$$

where N_i is the molar flow rate of permeating component *i* (mol s^{-1}), A is the effective membrane area (m^2), and ΔP_i is the transmembrane partial pressure difference of component *i* (Pa).

The mixed-gas separation factor α_{ij} was calculated as:

$$\alpha_{ij} = \frac{y_i/y_j}{x_i/x_j}$$

where x_i and x_j are the molar fractions of components i and j in the feed stream, respectively, while y_i and y_j are the corresponding molar fractions in the permeate stream.

The diffusivity coefficient (D) and solubility coefficient (S) of the membranes were determined using a constant-volume variable-pressure permeation apparatus via the pure-gas time-lag method at 298 K and a transmembrane pressure difference of 50 kPa. Before each measurement, both sides of the membrane cell were evacuated to remove residual gases. The downstream pressure increase was then recorded after introducing the test gas to the feed side, and D and S were calculated from the time-lag analysis.

The diffusion coefficient (D, $cm^2\ s^{-1}$) was calculated using the time-lag method according to:

$$D = \frac{l^2}{6\theta}$$

where l is the membrane thickness (cm), and θ is the time lag (s) obtained from the intercept of the steady-state downstream pressure rise curve.

Supplementary Figures

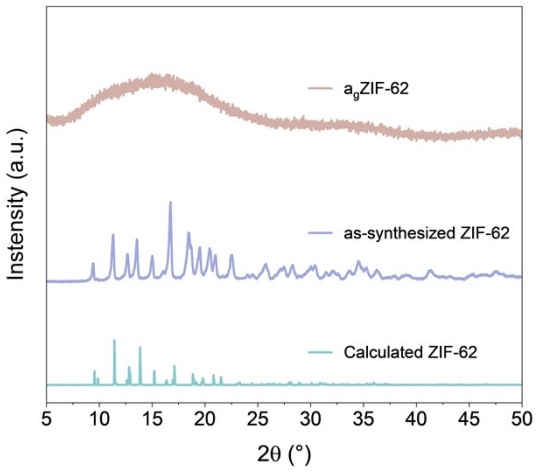

Fig. S1 XRD spectra of pure ZIF-62 crystal and ZIF-62 glass.

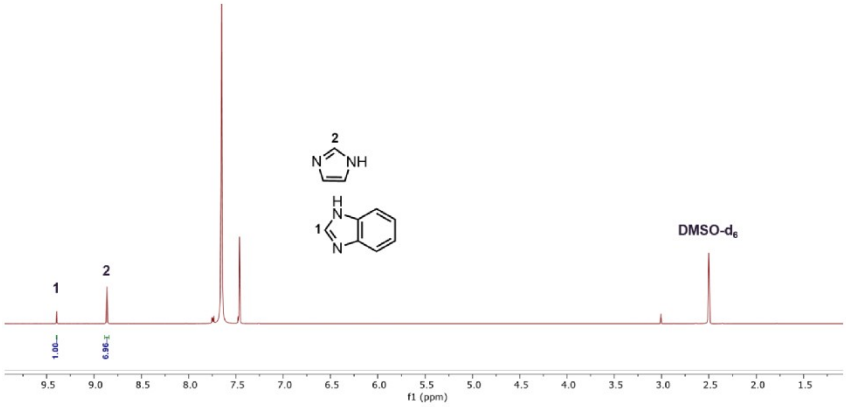

Fig. S2 ^{1}H NMR spectrum of ZIF-62-bIm$_{0.25}$ digested in DCl/DMSO-d$_6$.

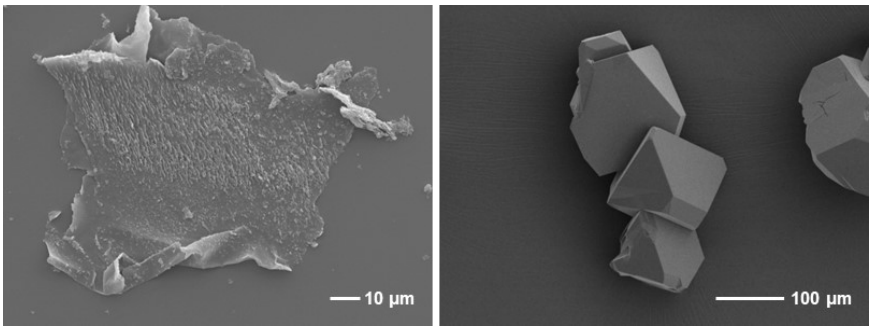

Fig. S3 SEM of g-C_3N_4 and ZIF-62 crystal.

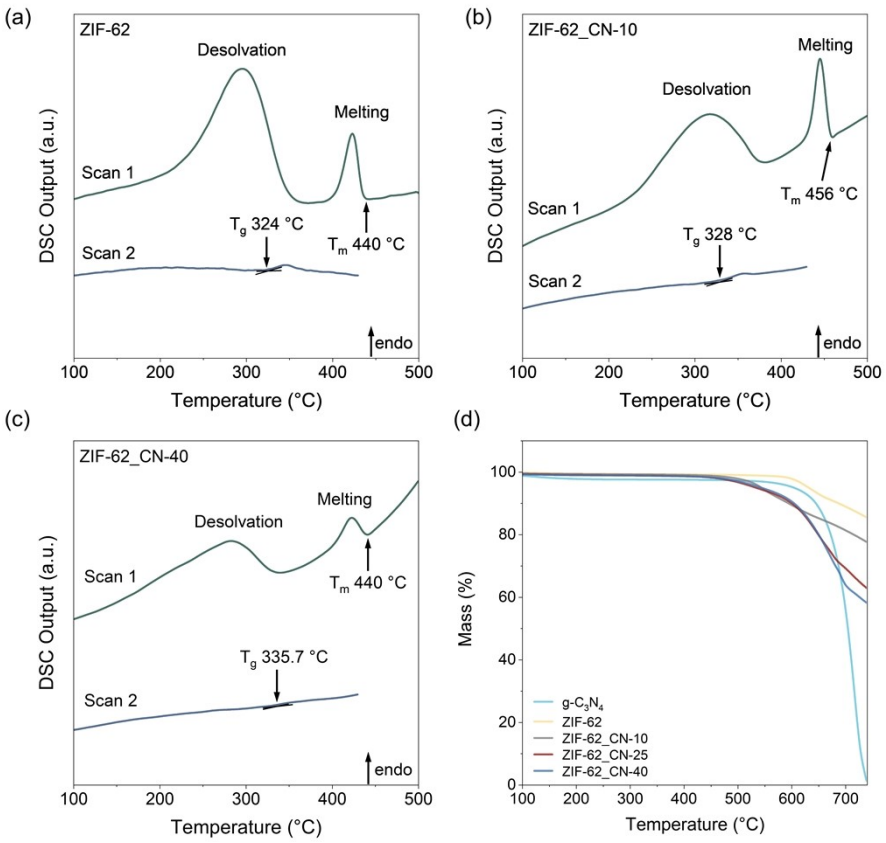

Fig. S4 (a) DSC curves of ZIF-62 crystal. (b) DSC curves of ZIF-62_CN-10 composite. (c) DSC curves of ZIF-62_CN-40 composite. (d) TG curve of ZIF-62, g-C_3N_4, ZIF-62_CN-10, ZIF-62_CN-25, ZIF-62_CN-40.

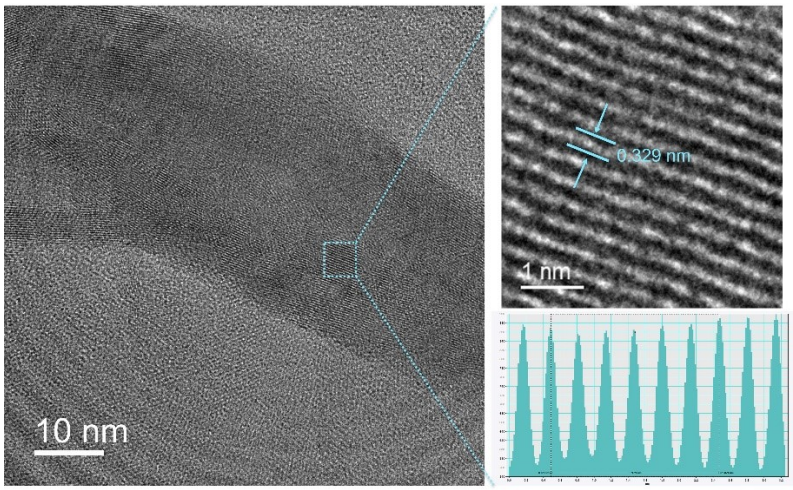

Fig. S5 High-resolution TEM image of pure g-C_3N_4 and its line profile analysis extracted from the HRTEM image, illustrating the periodic contrast with apparent spacing.

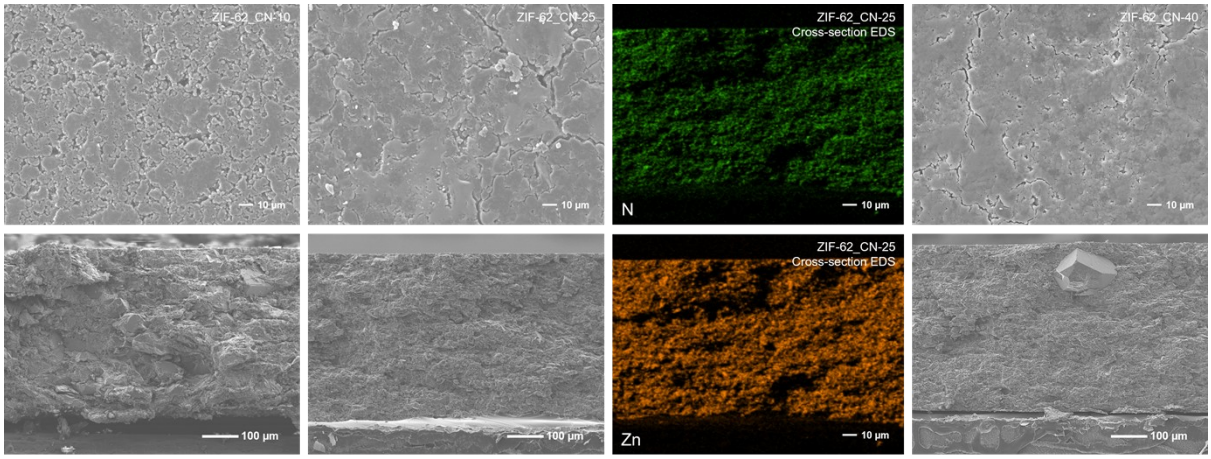

Fig. S6 SEM images of CGC membrane surfaces and cross-section before melting and EDS of ZIF-62_CN-25 pellet.

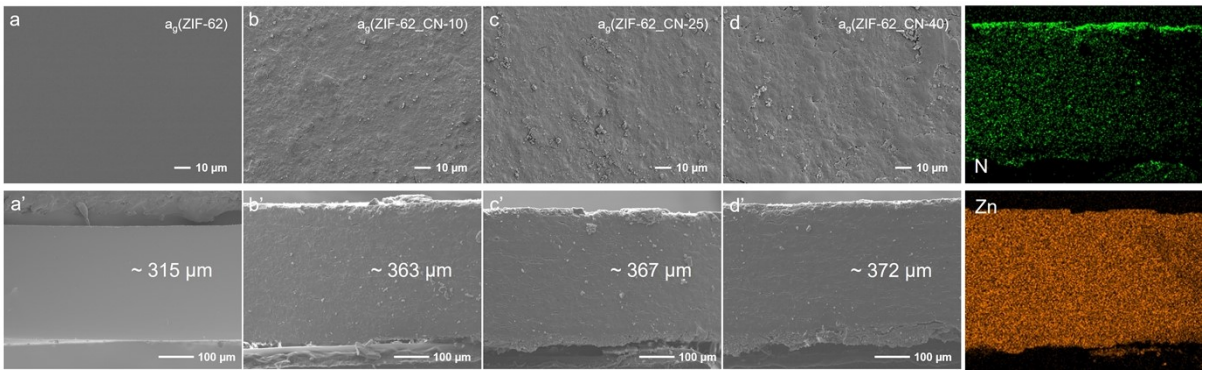

Fig. S7 SEM images of CGC membrane surfaces and cross-section after melting of a_gZIF-62_CN-25 pellet with EDS. (a, a') a_gZIF-62. (b, b') a_gZIF-62_CN-10. (c, c') a_gZIF-62_CN-25. (d, d') a_gZIF-62_CN-40

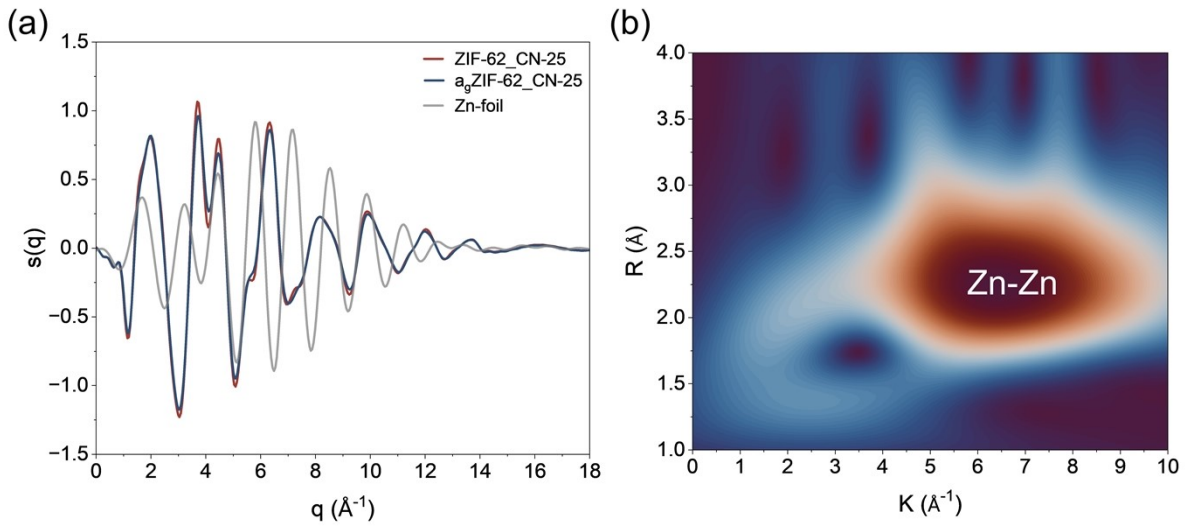

Fig. S8 (a) X-ray scattering factors (s) for ZIF-62_CN-25 and a_gZIF-62_CN-25 determined from total scattering data, q is the scattering vector. (b) Full-range wavelet transform (WT) representation for the Zn K edge of Zn foil.

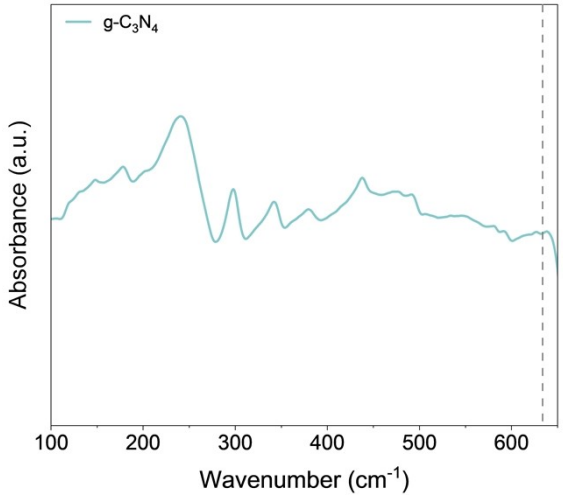

Fig. S9 THz/far-IR spectra of pure g-C_3N_4.

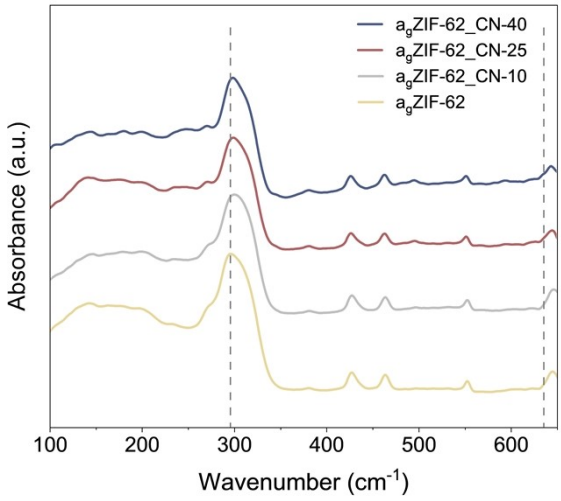

Fig. S10 Ex-situ THz/far-IR spectra of a_gZIF-62 and a_gZIF-62_CN-x glass composites.

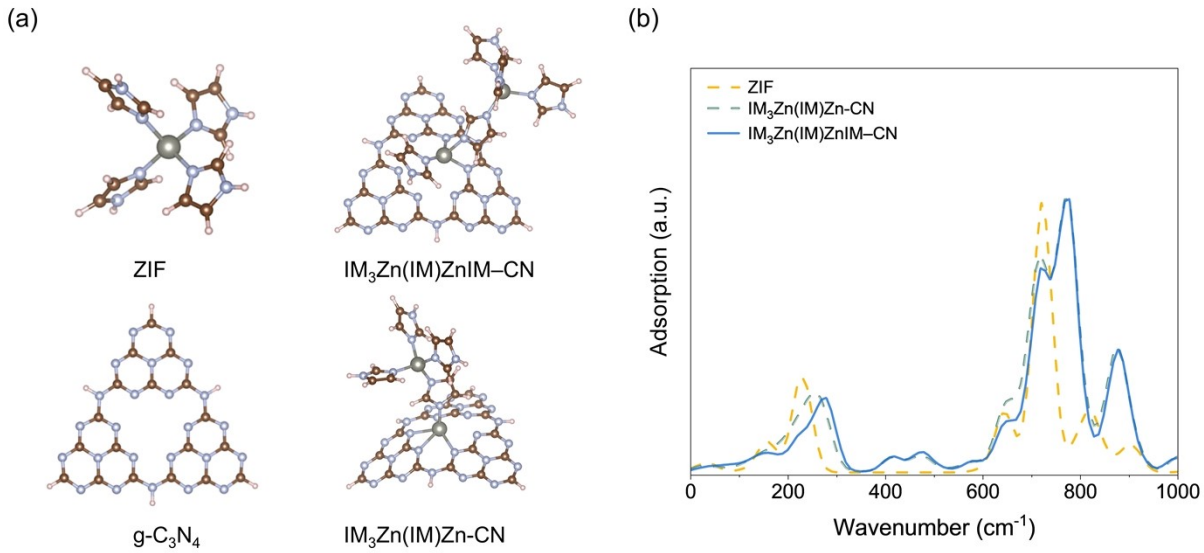

Fig. S11 DFT calculated $IM_3Zn(IM)Zn$-CN and $IM_3Zn(IM)ZnIM$-CN tetrahedron spectra in the wavenumber range to 1000 cm^{-1}, with the schematic diagram of the corresponding vibrational movements for DFT calculation at 298 K. Zn, grey; C, brown; N, blue; and H, pink.

The DFT cluster models are used here to probe local Zn coordination geometry and short-range vibrational features associated with interfacial Zn–N interactions. We note that these finite cluster models do not fully capture long-wavelength collective phonon modes in the bulk glass. Therefore, the qualitative agreement between the calculated and experimental spectra is

interpreted as evidence for local bonding changes and Zn-centred structural distortion, rather than a complete description of the bulk THz/FarIR vibrational response. According to the above DFT result, we find that a considerable size dependence on the ZIF-only models, indicating that a much larger cluster would be required to reach convergence. However, for the CN and ZIF-CN models, the calculated vibrational band within the window of interest depends only mildly on the system size. Therefore, the CN and ZIF-CN systems were chosen for further analysis owing to their seemingly better numerical reliability. The results presented in the results correspond to medium-sized systems with up to ~100 atoms. In all cases, the geometries were fully optimized, and the vibrational frequencies and intensities were obtained with the same quantum chemistry method in conjunction with the harmonic approximation. For the pure CN model, the absorption band in the 0-400 cm^{-1} range centers around 260 cm^{-1}. When a ZIF model interacts partially with the CN model to form $IM_3Zn(IM)ZnIM$-CN, this band shifts only slightly towards higher wavenumber. However, when the interacting Zn is fully in the hole of the CN model, i.e., $IM_3Zn(IM)Zn$–CN, a more considerable shift (to ~280 cm^{-1}) is observed, which is qualitatively consistent with the experimental observation.

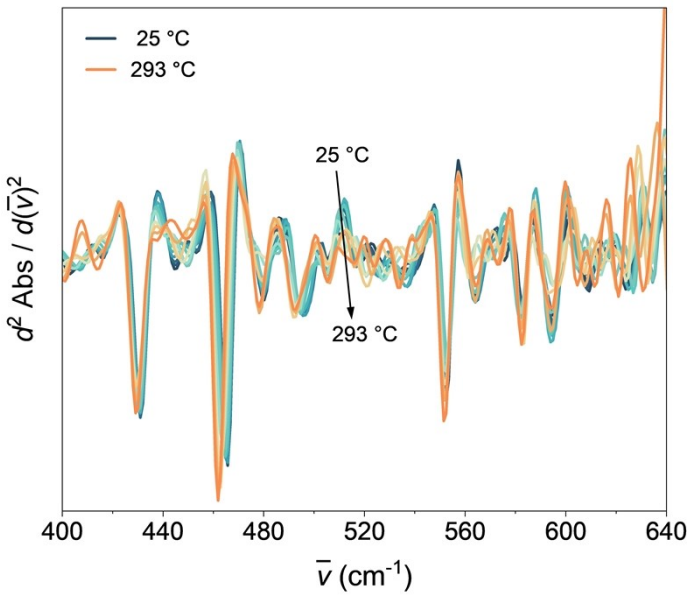

Fig. S12 The second derivative of the spectra highlighting the emergence of a hump peak around 600~640 cm^{-1} after melt-quenching.

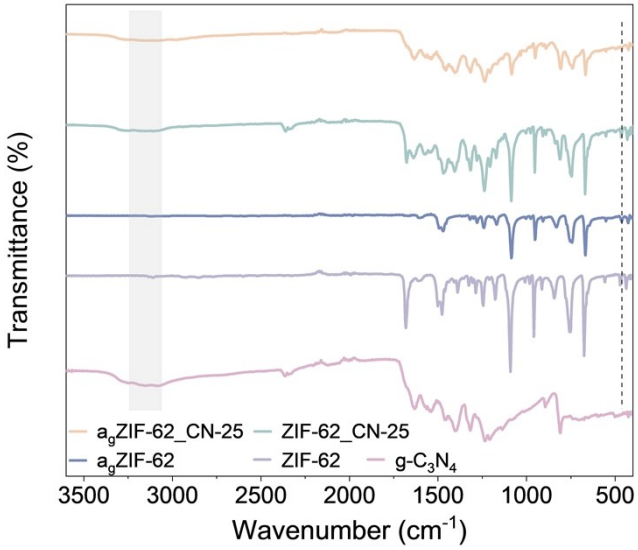

Fig. S13 FTIR spectra of ZIF-62, a_gZIF-62, ZIF-62_CN-25, a_gZIF-62_CN-25, g-C_3N_4.

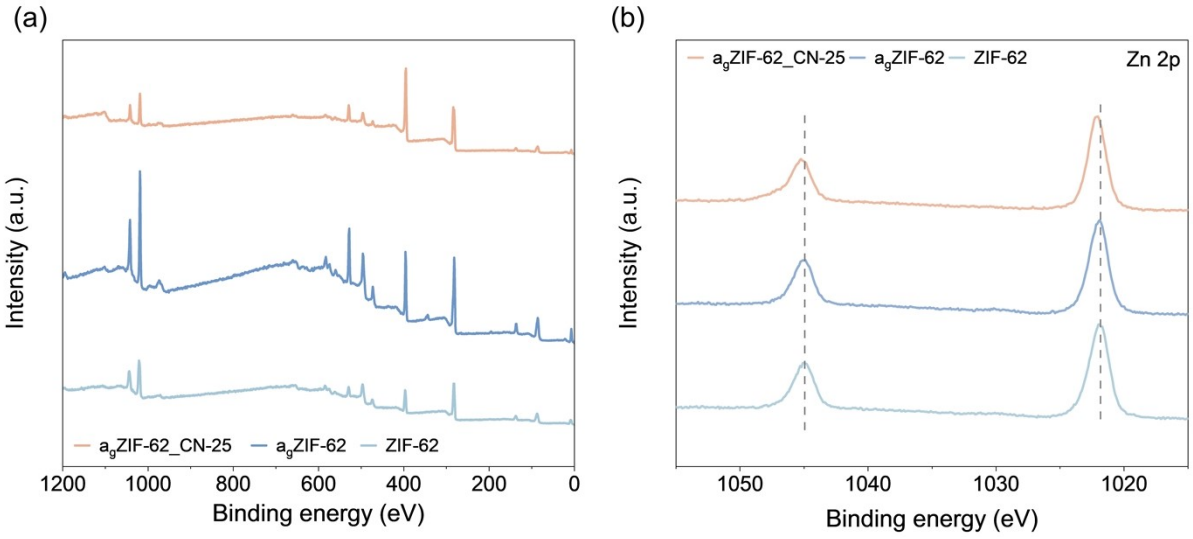

Fig. S14 XPS full spectra and Zn 2p spectra for ZIF-62, a_gZIF-62, a_gZIF-62_CN-25.

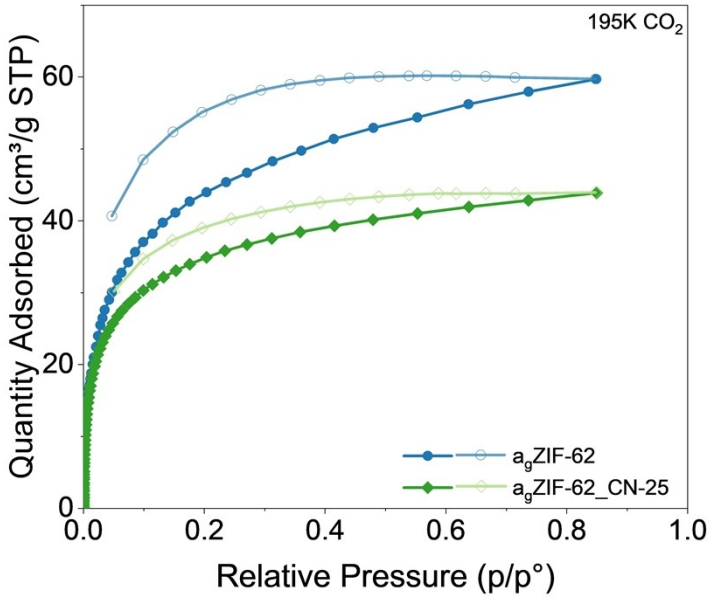

Fig. S15 The BET test with CO_2 adsorption isotherm curves at 195K of a_gZIF-62, a_g ZIF-62_CN-25.

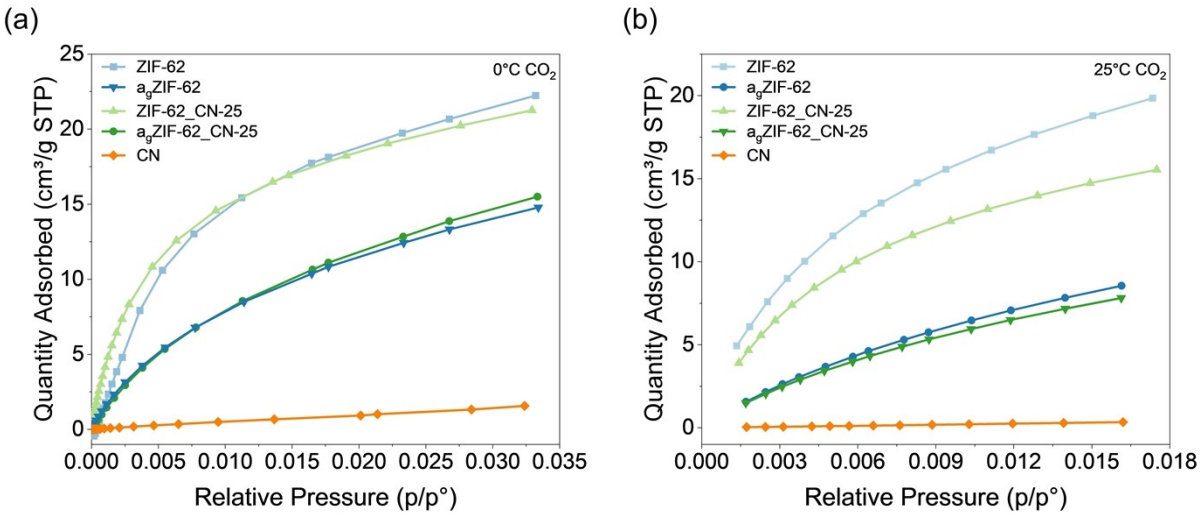

Fig. S16 CO_2 adsorption isotherm curves at (a) 273K (b)298K of ZIF-62, g-C_3N_4, ZIF-62_CN-25, a_gZIF-62, a_gZIF-62_CN-25.

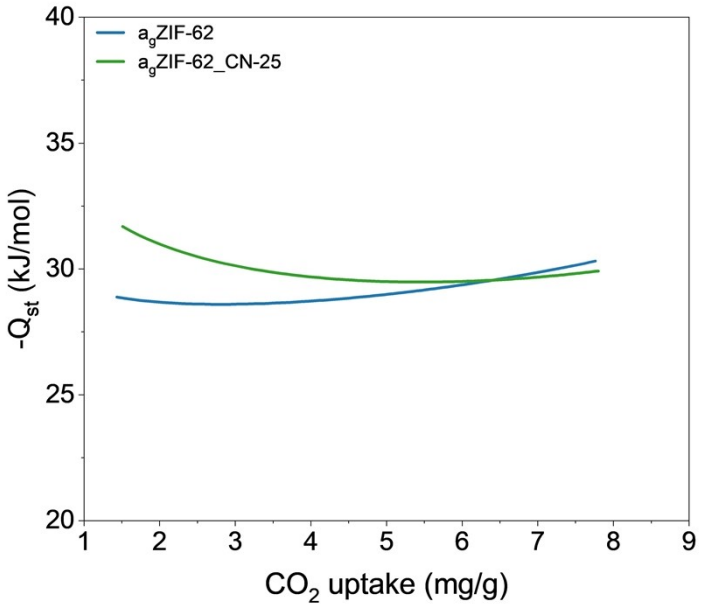

Fig. S17 Heat of CO_2 adsorption for a_g ZIF-62 and a_gZIF-62_CN-25 calculated from 273K and 298K.

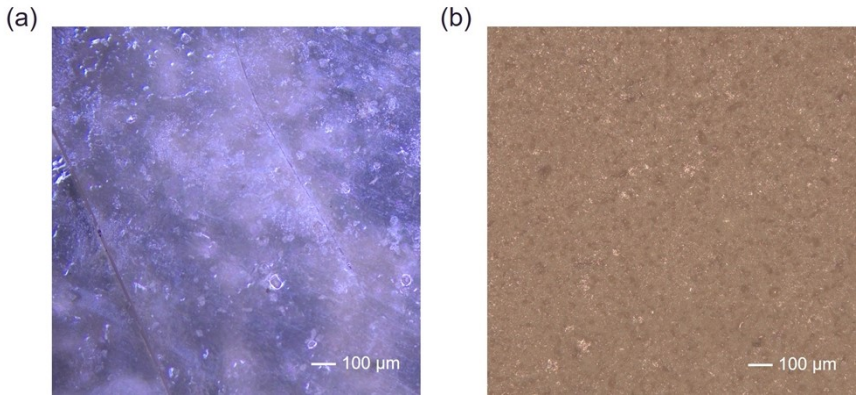

Fig. S18 Optical microscope images of (a) pure a_gZIF-62 and (b) a_gZIF-62_CN-25 pellets prepared under identical sintering conditions.

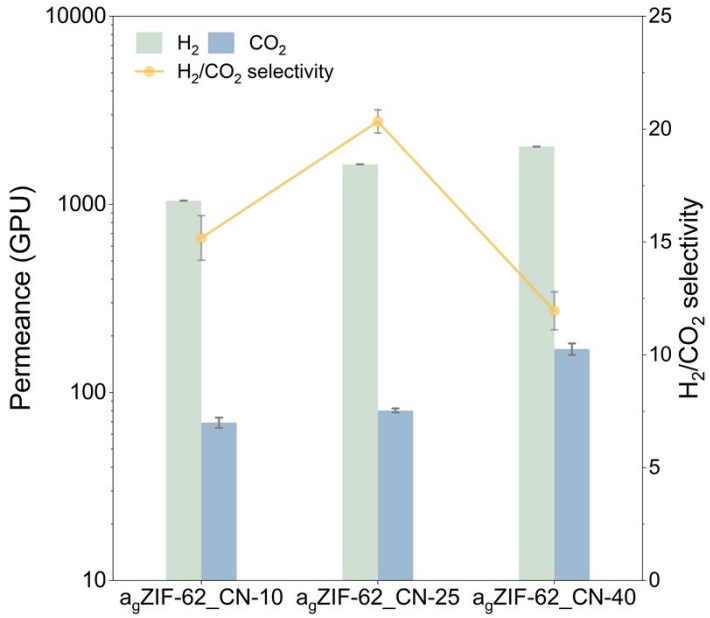

Fig. S19 Permeance and separation factors of the glass composite membranes in the equimolar mixed-gas permeation at room temperature.

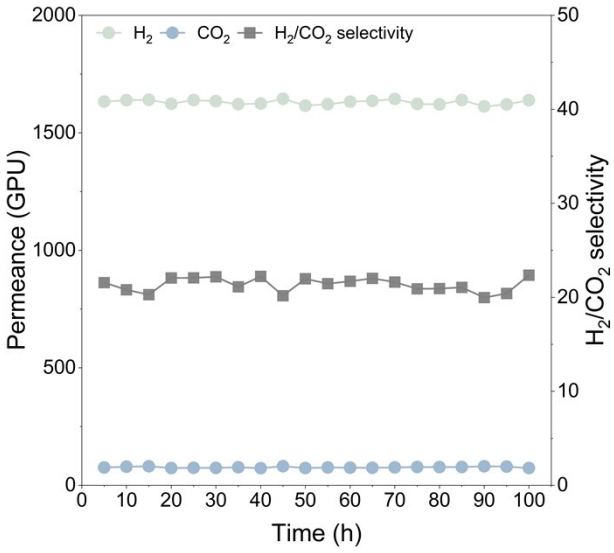

Fig. S20 Extended time gas separation performance stability of the a_gZIF-62_CN-25 membrane with H_2/CO_2 mixed gas (50/50 by volume) at room temperature.

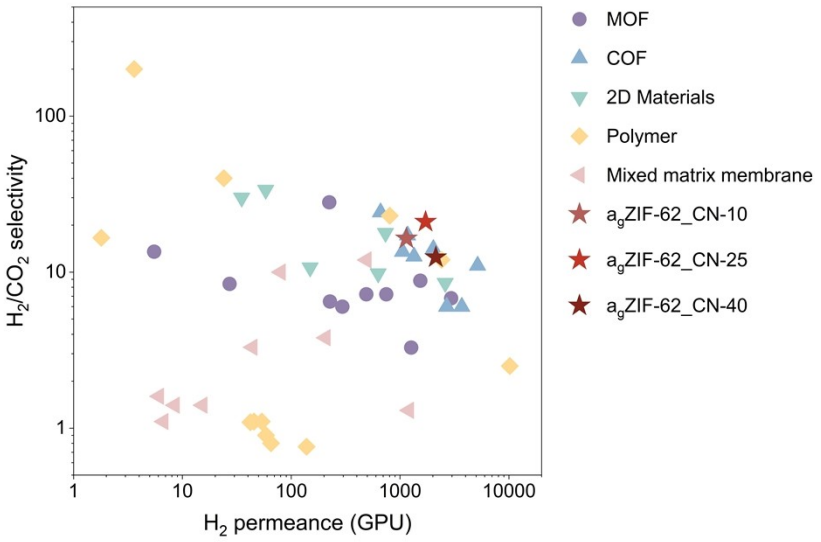

Fig. S21 Comparison of H_2/CO_2 separation performance of glass composite membranes with state-of-the-art membranes at room temperature.

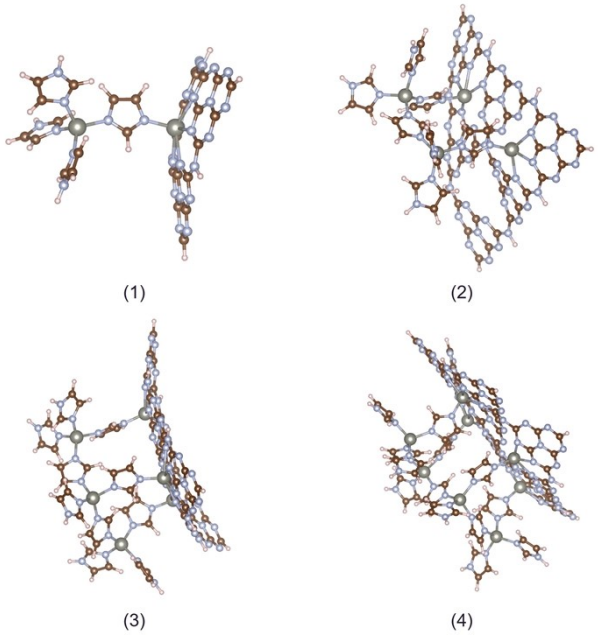

Fig. S22 DFT cluster models with increased structural size giving different local Zn-N distances in Table S3

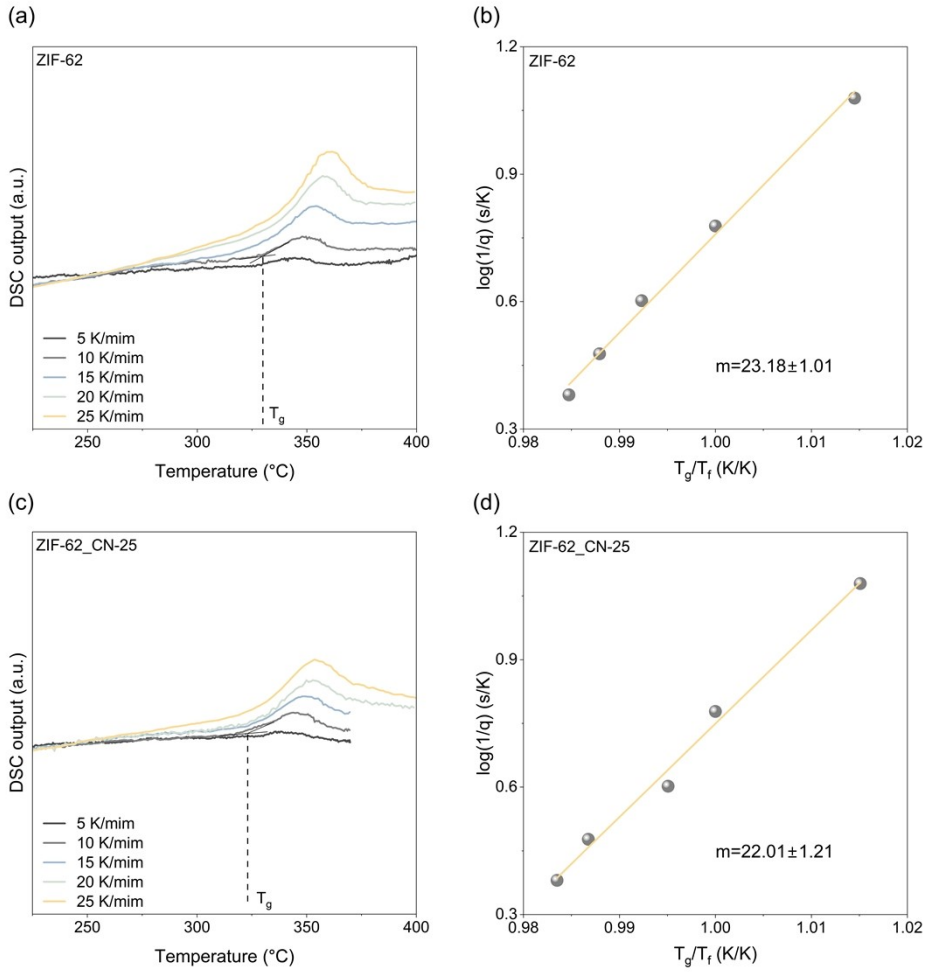

Fig. S23 DSC curves collected at different heating rates (5–25 K min^{-1}) for (a) pristine a_gZIF-62 and (c) a_gZIF-62_CN-25 used for fragility analysis. Corresponding Angell plots of $\log(q^{-1})$ versus T_g/T_f for (b) a_gZIF-62 and (d) a_gZIF-62_CN-25, yielding fragility indices (m) of 23.18 ± 1.01 and 22.01 ± 1.21, respectively. The slightly reduced fragility after g-C_3N_4 incorporation suggests moderately suppressed structural relaxation dynamics and slightly stronger glass-forming behaviour in the composite system.

Supplementary Tables

Table. S1 EXAFS fitting parameters at the Zn K-edge.

	shell	Coordination number	R (Å)	σ^2	R factor
ZIF-62_CN-25	Zn-N	3.9 ±0.3	1.99	0.0046	0.0154
	Zn-C	3.3 ±0.9	3.00	0.0042	
a_gZIF-62_CN-25	Zn-N	3.8±0.3	1.99	0.0048	0.0098
	Zn-C	2.9±1.1	3.01	0.0064	
	Zn-Zn	0.367	2.5	0.0139	

Table. S2 Single gas permeance for a_gZIF-62_CN-x CGC, under 1 bar 30 °C.

Permeance (GPU)	a_gZIF-62	a_gZIF-62_CN-10	a_gZIF-62_CN-25	a_gZIF-62_CN-40
H_2	14.93	1143.65	1716.01	2133.50
CO_2	2.08	69.64	81.67	171.33
N_2	4.10	99.65	117.60	222.28
H_2/CO_2 Selectivity	7.18	16.42	21.01	12.45

Table.S3 Local Zn-N distances environment with four DFT cluster models in Fig. S22.

Zn-N distances in the holes	1	2	3	4
Max	2.438	2.596	2.678	2.720
Min	2.378	2.208	2.175	2.170
Range	0.060	0.389	0.503	0.550
SD	0.023	0.139	0.187	0.188

Table S4. Gas permeability and apparent diffusivity coefficient.

Membrane	Permeability (10^4 barrer)		Apparent diffusivity coefficient (10^{-8} m^2/s)	
	H_2	CO_2	H_2	CO_2
a_gZIF-62	0.569	0.079	1.342	0.434
a_gZIF-62_CN-10	43.573	2.653	4.293	1.496
a_gZIF-62_CN-25	65.380	3.112	7.441	1.761
a_gZIF-62_CN-40	81.286	6.528	10.618	2.594

Table. S5 H_2/CO_2 separation performances of the state-of-the-art membranes tested under transmembrane pressure 1 bar and room temperature.

Category	**Membrane**	**H_2 permeance (GPU)**	**H_2/CO_2 selectivity**	**Ref**
MOF	HKUST-1	2947.4	6.8	[5]
	ZIF-7	27.1	8.4	[6]
	ZIF-7	227.2	6.48	[7]
	ZIF-22	489.3	7.2	[8]
	ZIf-8	294.7	6	[9]
	ZIF-8	1267.4	3.28	[10]
	Amine-Mg-MOF-74	224	28	[11]
	MIL-96(Al)	1532.6	8.8	[12]
	ZIF-7-II/OPBI	5.5	13.5	[13]
COF	COF-300	5160	11	[14]
	[COF-300]-[Zn2(bdc)2(dabco)])	1344	12.6	[15]
	[COF-300]-[ZIF-8]	1055.2	13.5	[15]
	COF-300	2688	6	[15]
	COF-LZU1	3684.2	6	[16]
	ACOF-1	2018.9	14.1	[16]
	COF-LZU1-ACOF-1	660.2	24.2	[16]
	[COF-300]-[UiO-66]	1173.1	17.2	[17]
2D	Mxene-95 (RH=10%)	733.4	17.8	[17]
	Mxene (RH=40%)	628.7	9.8	[17]
	NiAl-CO3 LDH	1.49E+02	10.7	[18]
	GO	35	30	[19]
	TU-GOF-1	2603	8.5	[20]
	BNG	58.3	33.6	[21]
Polymer	PIM-EA-TB	42.1	1.09	[22]
	PIM-SBI-TB	138.2	0.76	[22]
	EDA-polyimide	1.8	16.6	[23]
	PBI-HFA	10198	2.5	[24]

	Torlon®/PEEI/PAA	3.6	200	[25]
	PIM-1	1.63	0.3	[26]
	CoPIM-TB (90:10)	65.34	0.8	[27]
	CoPIM-TB (80:20)	58.73	0.9	[27]
	CL-CoPIM-TB (90:10)	53.73	1.1	[27]
	CL-CoPIM-TB (80:20)	45.6	1.1	[27]
	BILP	24	40	[28]
	PBDI	803.3333333	23	[29]
	AO-PIM-1	2410.169492	12	[30]
MMM	NUS-2@PBI	0.059	18.78	[31]
	m-PBI	80	10	[32]
	PIM-1/ZIF-8	6.68	1.1	[26]
	6FDA-DAM:DABA (3:2)/ZIF-8	8.48	1.4	[33]
	6FDA-DAM:DABA (3:2)/ZIF-8-NH_2	15.24	1.4	[33]
	PES/NU-1000-GNs	44.025	3.3	[34]
	PC/KAP	0.38411215	1.3	[35]
	PC/KAP-NO_2	0.200735294	1.2	[35]
	PC/KAP-CH_2 NH_2	0.141666667	1.4	[35]
	HPI/ZIF-8 (80:20)	6.083333333	1.6	[36]
	TR-PBOI/ZIF-8 (80:20)	1206	1.3	[36]
	6FDA-DAM/ZIF-7-III (97.2:2.8)	206.3291139	3.8	[37]
	AO-PIM-1@ZIF-8	491.4705882	11.97	[30]

Supplementary References

1 C. Bannwarth, E. Caldeweyher, S. Ehlert, A. Hansen, P. Pracht, J. Seibert, S. Spicher and S. Grimme, *WIREs Computational Molecular Science*, 2021, **11**, e1493.

2 C. Bannwarth, S. Ehlert and S. Grimme, *J. Chem. Theory Comput.*, 2019, **15**, 1652–1671.

3 M. Müller, A. Hansen and S. Grimme, *The Journal of Chemical Physics*, 2023, **158**, 014103.

4 F. Neese, *WIREs Comput Mol Sci*, 2022, **12**, e1606.

5 H. Guo, G. Zhu, I. J. Hewitt and S. Qiu, *J. Am. Chem. Soc.*, 2009, **131**, 1646–1647.

6 Y.-S. Li, H. Bux, A. Feldhoff, G.-L. Li, W.-S. Yang and J. Caro, *Advanced Materials*, 2010, **22**, 3322–3326.

7 Y.-S. Li, F.-Y. Liang, H. Bux, A. Feldhoff, W.-S. Yang and J. Caro, *Angewandte Chemie International Edition*, 2010, **49**, 548–551.

8 A. Huang, H. Bux, F. Steinbach and J. Caro, *Angewandte Chemie International Edition*, 2010, **49**, 4958–4961.

9 H. Bux, A. Feldhoff, J. Cravillon, M. Wiebcke, Y.-S. Li and J. Caro, *Chem. Mater.*, 2011, **23**, 2262–2269.

10 K. Huang, Z. Dong, Q. Li and W. Jin, *Chem. Commun.*, 2013, **49**, 10326–10328.

11 N. Wang, A. Mundstock, Y. Liu, A. Huang and J. Caro, *Chemical Engineering Science*, 2015, **124**, 27–36.

12 A. Knebel, S. Friebe, N. C. Bigall, M. Benzaqui, C. Serre and J. Caro, *ACS Appl. Mater. Interfaces*, 2016, **8**, 7536–7544.

13 S. Yang, Y. Wang, P. Lu, H. Jin, F. Pan, Z. Shi, X. Jiang, C. Chen, Z. Jiang and Y. Li, *ACS Appl. Mater. Interfaces*, 2020, **12**, 55308–55315.

14 B. Li, Z. Wang, Z. Gao, J. Suo, M. Xue, Y. Yan, V. Valtchev, S. Qiu and Q. Fang, *Advanced Functional Materials*, 2023, **33**, 2300219.

15 J. Fu, S. Das, G. Xing, T. Ben, V. Valtchev and S. Qiu, *J. Am. Chem. Soc.*, 2016, **138**, 7673–7680.

16 H. Fan, A. Mundstock, A. Feldhoff, A. Knebel, J. Gu, H. Meng and J. Caro, *J. Am. Chem. Soc.*, 2018, **140**, 10094–10098.

17 S. Das and T. Ben, *Dalton Trans.*, 2018, **47**, 7206–7212.

18 Y. Liu, N. Wang and J. Caro, *J. Mater. Chem. A*, 2014, **2**, 5716–5723.

19 N. Y. Oh, S. Y. Lee, J. Lee, H. J. Min, S. S. Hosseini, R. Patel and J. H. Kim, *Polymers*, DOI:10.3390/polym16212998.

20 J. Yang, D. Gong, G. Li, G. Zeng, Q. Wang, Y. Zhang, G. Liu, P. Wu, E. Vovk, Z. Peng, X. Zhou, Y. Yang, Z. Liu and Y. Sun, *Advanced Materials*, 2018, **30**, 1705775.

21 R. Wang, J. Qian, X. Chen, Z.-X. Low, Y. Chen, H. Ma, H.-A. Wu, C. M. Doherty, D. Acharya, Z. Xie, M. R. Hill, W. Shen, F. Wang and H. Wang, *Nat Commun*, 2023, **14**, 2161.

22 M. Carta, R. Malpass-Evans, M. Croad, Y. Rogan, J. C. Jansen, P. Bernardo, F. Bazzarelli and N. B. McKeown, *Science*, 2013, **339**, 303–307.

23 L. Shao, C.-H. Lau and T.-S. Chung, *International Journal of Hydrogen Energy*, 2009, **34**, 8716–8722.

24 D. Y. Kim, S. Ryu, H.-J. Kim, H. C. Ham, H. Sohn, S. P. Yoon, J. Han, T.-H. Lim, J. Y. Kim, S. W. Lee, C. W. Yoon and S. H. Choi, *Separation and Purification Technology*, 2021, **257**, 117954.

25 N. K. Mishra, N. Patil, C. Long, S. Yi, D. Hopkinson, J. C. Grunlan and B. A. Wilhite, *Journal of Membrane Science*, 2020, **615**, 118312.

26 A. F. Bushell, M. P. Attfield, C. R. Mason, P. M. Budd, Y. Yampolskii, L. Starannikova, A. Rebrov, F. Bazzarelli, P. Bernardo, J. Carolus Jansen, M. Lanč, K. Friess, V. Shantarovich, V. Gustov and V. Isaeva, *Journal of Membrane Science*, 2013, **427**, 48–62.
27 C. Zhang, L. Fu, Z. Tian, B. Cao and P. Li, *Journal of Membrane Science*, 2018, **556**, 277–284.
28 M. Shan, X. Liu, X. Wang, I. Yarulina, B. Seoane, F. Kapteijn and J. Gascon, *Science Advances*, 2018, **4**, eaau1698.
29 M. Shan, X. Liu, X. Wang, Z. Liu, H. Iziyi, S. Ganapathy, J. Gascon and F. Kapteijn, *J. Mater. Chem. A*, 2019, **7**, 8929–8937.
30 S. Xiong, C. Pan, G. Dai, C. Liu, Z. Tan, C. Chen, S. Yang, X. Ruan, J. Tang and G. Yu, *Journal of Membrane Science*, 2022, **645**, 120217.
31 Z. Kang, Y. Peng, Y. Qian, D. Yuan, M. A. Addicoat, T. Heine, Z. Hu, L. Tee, Z. Guo and D. Zhao, *Chem. Mater.*, 2016, **28**, 1277–1285.
32 L. F. Villalobos, R. Hilke, F. H. Akhtar and K.-V. Peinemann, *Advanced Energy Materials*, 2018, **8**, 1701567.
33 J. H. Jo, C. O. Lee, G. Y. Ryu, H. Jae, D. Roh and W. S. Chi, *ACS Appl. Polym. Mater.*, 2022, **4**, 6426–6439.
34 A. Mohamed, S. Yousef, V. Makarevicius and A. Tonkonogovas, *International Journal of Hydrogen Energy*, 2023, **48**, 19596–19604.
35 L. Rodríguez-Jardón, M. López-González, M. Iglesias and E. M. Maya, *Journal of Membrane Science*, 2021, **619**, 118795.
36 J. S. Kim, S. J. Moon, H. H. Wang, S. Kim and Y. M. Lee, *Journal of Membrane Science*, 2019, **582**, 381–390.
37 S. Park, K. Y. Cho and H.-K. Jeong, *J. Mater. Chem. A*, 2020, **8**, 11210–11217.